Wet-Chemical Synthesis of Enhanced-Thermopower $Bi_{1-x}Sb_x$ Nanowire Composites for Solid-State Active Cooling of Electronics

K. Vandaele,[1,2] Bin He,[1] P. Van Der Voort,[2] K. De Buysser,[2] and J. P. Heremans[1,3,4]

[1]*Department of Mechanical and Aerospace Engineering, Columbus, Ohio 43210, USA*
[2]*Department of Chemistry, Ghent University, Krijgslaan 281—S3, 9000 Gent, Belgium*
[3]*Department of Physics, The Ohio State University, Columbus, Ohio 43210, USA*
[4]*Department of Materials Science and Engineering, The Ohio State University, Columbus, Ohio 43210, USA*

(Received 31 July 2017; revised manuscript received 1 December 2017; published 20 February 2018)

This paper is a contribution to the Physical Review Applied *collection in memory of Mildred S. Dresselhaus.*

In 1993, Hicks and Dresselhaus [Thermoelectric figure of merit of a one-dimensional conductor, Phys. Rev. B **47**, 16631 (1993).] suggested that Bi nanowires could result in values of the thermoelectric figure of merit $zT > 1$. The Dresselhaus group also calculated a ternary phase diagram for $Bi_{1-x}Sb_x$ nanowires as a function of x and wire diameter. This manuscript reports a wet-chemical method to synthesize $Bi_{1-x}Sb_x$-silica nanowire composites. Resistivity, Hall electron concentration, electron mobility, Seebeck and Nernst coefficients, and thermal conductivity of composites are measured and compared to bulk polycrystalline $Bi_{1-x}Sb_x$ samples prepared either by ingot casting or by the same wet chemistry but without nanostructuring. A clear increase of the thermopower in 20-nm $Bi_{94}Sb_6$-silica is reported when compared to bulk samples, and the values are among the highest found in the literature from 300 to 380 K, even though the electron concentration is higher than in the bulk. This suggests that consistent with theory, size quantization is responsible for the thermopower increase.

DOI: 10.1103/PhysRevApplied.9.024020

I. INTRODUCTION

Peltier-effect-based solid-state cooling possesses many advantages over conventional cooling provided by thermodynamic cycles, namely, vibration-free operation from the absence of moving parts, a long lifetime, reliability, and compactness. Further, if we consider an ideal heat exchanger, thermoelectric (TE) devices have an extremely high specific cooling capacity. TE devices also have a short thermal response time. Their efficiency (today equivalent to 25% of that of vapor-compression coolers) is determined by the TE figure of merit of the materials zT, which depends on thermal conductivity κ, electrical conductivity σ, and Seebeck coefficient α. Note that zT refers to the materials' figure of merit, whereas ZT is the device's figure of merit (contribution of n-type and p-type legs). Together with the absolute temperatures of the hot side and the cold side of a TE energy converter (which determine its Carnot efficiency), the figure of merit zT of the TE materials governs its thermal efficiency. Here, $zT \equiv \alpha^2\sigma T/\kappa$, where α is the thermopower of the material, κ and σ are its thermal and electrical conductivities, respectively, and T is the average temperature. By separating the electronic (κ_E) and lattice (κ_L) thermal conductivities and applying the Wiedemann-Franz-Lorenz law ($\kappa_E = LT\sigma$, where $L \approx 1.6$ to 2.5×10^{-8} V^2/K^2 is the Lorenz ratio), the figure of merit becomes $zT = \alpha^2/L[1 + (\kappa_L/\kappa_E)]^{-1}$. This illustrates how important it is to maximize α and how only κ_L should be minimized, whereas a high κ_E is actually beneficial to zT.

The vast majority of applications for TE technology are in cooling applications such as automotive climate control via cooled seats, medical and scientific instrumentation, and camping gear. A large expansion of these applications into active TE cooling for thermal management of electronic circuits and batteries might be possible if the zT were enhanced enough and the materials cost sufficiently controlled. Choosing between active TE cooling and passive cooling of such devices depends on the ratio between the required device temperature T_d and the temperature T_a at which the heat can be rejected. Active TE cooling implies that the heat exchanger system must handle not only the heat load from the device but also that generated by the TE device itself, which is related to the TE figure of merit of the device (ZT). In the Supplemental Material [1], we show how this consideration imposes the condition

$$T_d < T_a \frac{1 + \sqrt{1 + ZT}}{2}. \tag{1}$$

Only if condition (1) is met will an active TE cooler be more compact than a passive cooler. Given the importance of heat management to developing batteries and electronic

circuits, zT improvements for cooling materials could have great technological impact. Cryogenic coolers are another potential field of application. Today's six-stage Peltier coolers can reach temperatures as low as 170 K for a hot side of 300 K. Enhancements in the material's zT below room temperature could impact the cooling of IR detectors and other sensors in which thermal noise must be minimized by keeping them at temperatures below ambient.

Unfortunately, the interdependence of the material properties determining zT and their counterindicated nature makes it difficult to increase zT. By far, the best cooling materials near room temperature are tetradymites, generally $(Bi_{1-x}Sb_x)_2(Te_{1-y}Se_y)_3$ compound semiconductors that crystallize with the $\bar{3}m$ space group. This is because the strong spin-orbit coupling in those compounds results in a very high electron mobility, while the high degeneracy of the pockets that form the Fermi surface result in a favorable thermopower [2]. The same arguments hold for $Bi_{1-x}Sb_x$ alloys. These are particularly suitable below room temperature. Until now, they have not been considered seriously for applications because, in bulk, they must be used as mechanically fragile single crystals. Preparing bulk $Bi_{1-x}Sb_x$ TEs is also difficult because the large temperature difference between the liquidus and solidus impedes the reasonably accurate control of x [3]. The wet-chemistry route described here circumvents this problem.

Hicks and Dresselhaus predicted that zT would be enhanced greatly in quantum-well [4] and wire [5] structures because size-quantization effects result in a sharpening of the features of the density of states (DOS), in turn, increasing the thermopower. Because of its charge carriers' small effective mass, particularly electrons [6–8], elemental Bi was the chosen paradigm for this effect.

Bulk Bi is a semimetal [9] with valence bands (VB) centered around the Brillouin zone (BZ) T points; the Fermi level cuts these VBs about 11 meV below their extremum. Conduction bands are centered at the BZ L points with L_s symmetry, which cut the Fermi energy approximately 27 meV above their minimum, leading to an energy overlap of $E_{gTLs} = -38$ meV (a positive value indicates a band gap; an energy overlap is treated as a negative band gap) [9]. Also at the L point, there is a VB of L_a symmetry separated from the L_s band by a direct energy gap $E_{gLsa} = 13.6$ meV [6]. In semimetals, the electron and hole partial thermopowers counter each other; thus, the overall thermopower is smaller than that of each separate carrier type, greatly reducing zT. Indeed, it was predicted that if we could lift the band overlap in bulk Bi and reduce the electron density at room temperature from the semimetals 3×10^{18} cm^{-3} to 1×10^{18} cm^{-3} in this hypothetical semiconductor, its zT could reach 1.3 [10]. Then, simply opening a gap by size quantization in the Bi electron band structure should result in a great zT improvement. A theoretical calculation [11] predicted that zT values >5 could be reached in 5-nm-diameter Bi nanowires via three effects: sharp features in the DOS energy dependence, opening a gap, and reducing lattice thermal conductivity. This promising result stimulated renewed TE research efforts [12].

Early experiments on Bi nanowires and nanowire composites proved the theory essentially correct. Two methods were developed to synthesize Bi nanowires inside porous media, typically silica or alumina: high-pressure injection [13] and *in situ* vapor growth. [14] It was shown experimentally [15] that confining Bi into nanowires resulted in the opening of a band gap, as predicted [11] for wire diameters of 49 nm and below, although the mobility was reduced [16]. The thermopower enhancement was observed experimentally in nanocomposites containing Bi nanowires with diameters decreasing from 50 to 9 nm [17,18].

Still, zT enhancement proved elusive. Thermal conduction through the porous matrix constitutes a thermal short [19], limiting the composite's effective zT. Because Bi oxidizes readily, sintered felts of nanowires extracted from their porous matrix cannot be measured; thus, this short cannot be avoided with today's technology. Mean free path limitations [20] increase the resistivity and affect zT negatively. Further, wires with diameters significantly below 10 nm display localization effects [18]. This is understood readily from the Anderson-Ioffe-Regel criterion for band conduction: the product of the Fermi wave vector k_F and the mean free path ℓ must obey $k_F l > 1$. For electrons in Bi, k_F is highly anisotropic, as shown by de Haas–van Alphen and Shubnikov–de Haas measurements [9] and show a lower bound of $k_F \approx 1 \times 10^8$ m^{-1}. Assuming that the wire diameter limits ℓ, localization is expected to appear for diameters around $k_F{}^{-1} \approx 10$ nm, as observed. In hindsight, this localization limits the applicability range of the early theoretical predictions.

Dresselhaus and co-worker suggested studying quantum wells [21], nanowires, and nanocomposites of $Bi_{1-x}Sb_x$ alloys. Sb is isoelectronic with Bi, and the alloys are solid solutions throughout the concentration range with no change in space group ($\bar{3}m$). Alloying Sb into Bi has three principal effects on its *bulk* band structure: with increasing Sb content, (i) the direct energy gap E_{gLsa} closes and ultimately inverts, (ii) the T-point hole band decreases in energy *vis-à-vis* the L-point bands, and (iii) the H-point VB increases in energy *vis-à-vis* the L-point bands [22].

Bulk single-crystal semiconducting $Bi_{1-x}Sb_x$ alloys yield the highest zT of all n-type materials at cryogenic temperatures when the fluxes are oriented along the trigonal axis [23,24]. Potassium is a resonant dopant in Bi and its alloys; a record $zT = 0.7$ was reported [25] at 100 K on K-doped $Bi_{95.5}Sb_{4.5}$, a composition near where the L-point bands have the Dirac dispersion. That sample yields $zT > 0.5$ from 40 to 300 K. p-type $Bi_{1-x}Sb_x$ alloys generally have lower zT values than n-type alloys, despite that Ga is a resonant acceptor in the material [26]. While the best materials still are single crystals, the best p-type materials' zT values are obtained when the fluxes are oriented in the

trigonal plane [27]. $Bi_{97}Sb_3$ is also one of the alloys best suited for Ettingshausen coolers [28]. Most bulk alloys give slightly better TE performance in Peltier and Ettingshausen geometries when the electron concentration is lowered by light, *p*-type counterdoping [29].

Dresselhaus and co-worker calculated size-quantization effects in $Bi_{1-x}Sb_x$ alloys for quantum wells [30] and wires [31]: size quantization and alloying effects cooperate to increase energy gaps. As a result, the semimetal-semiconductor transition occurring in 49-nm-diameter wires of elemental Bi or 9-at. % Sb in bulk $Bi_{1-x}Sb_x$ alloys occurs at lower Sb concentrations in nanostructures or at larger diameters in $Bi_{1-x}Sb_x$ than in Bi. The calculated (diameter, composition) phase diagrams are reported in Refs. [30,31]. By adding Sb to Bi, one can reasonably hope to increase the thermopower by size quantization in quantum wires of diameters substantially larger than the limit where localization effects occur. The present manuscript aims to show this experimentally.

Dresselhaus and co-workers pioneered the first experiments on 65-nm- and 40-nm-diameter $Bi_{1-x}Sb_x$ ($x = 0.05$–0.10) nanowires by using high-pressure injection synthesis [32], but they observed a more modest Seebeck coefficient enhancement than predicted, and the total thermopower remained significantly lower than single-crystal bulk alloys along the trigonal direction [29], reaching only $-60\ \mu V/K$ (100–300 K) for 45-nm $Bi_{0.95}Sb_{0.04}$ wires. The *in situ* vapor-deposition method was applied successfully to other elements, such as Sb [33] and Zn [34], but it was unsuccessful preparing $Bi_{1-x}Sb_x$ alloy nanowires due to the large vapor pressure difference between Bi and Sb.

II. EXPERIMENT

Here, we report on a wet-chemical synthesis route to prepare $Bi_{1-x}Sb_x$ nanowires that show enhanced thermopower compared to polycrystalline-equivalent alloys. The synthesis and characterization of elemental Bi nanowires using the same route as is used here for Bi-Sb alloys is described in detail in Ref. [35], and the same reference contains TEM analysis of Bi nanowires and transport measurements on elemental Bi nanowire composites, which are extended here to Bi-Sb-silica composites. In particular, temperature-dependent Hall measurements on a Bi nanowire-silica composite indicates a carrier concentration that increases as in an intrinsic semiconductor with an energy gap of 45 meV, which corresponds quite well with the prediction of Dresselhaus and co-workers [11] for 20-nm nanowires.

The wet-chemistry synthesis route given here applies to $Bi_{1-x}Sb_x$ alloy nanocomposites. Since these materials undergo a last heat treatment far below their melting point, they have a lower mobility than ingot-cast samples. Therefore, a comparison is made first between the galvanomagnetic (resistivity, Hall effect), thermomagnetic (Seebeck and Nernst coefficients), and thermal (thermal conductivity) properties of bulk $Bi_{1-x}Sb_x$ alloys synthesized via the conventional melt-casting process and those made by the wet-chemistry method used in the synthesis of the nanocomposites. The measurements of the properties of the bulk Bi-Sb samples prepared by the wet-chemistry method are then compared in the next section to similar measurements on chemically synthesized nanocomposites. We report a clear enhancement of the thermopower in nanowire composites of $Bi_{94}Sb_6$ at high temperature (250–400 K). This is particularly interesting because, in the existing literature, neither Sb content nor even extrinsic doping of Bi with acceptor or donor impurities is reported to affect the room-temperature thermopower of either Bi or Bi-rich Bi-Sb alloys significantly. The data reported here indicate that size confinements alter the room-temperature thermopower of Bi or Bi-rich Bi-Sb alloys in a particularly meaningful way, implying that size-quantization effects influence the band structure.

A. Materials

Hydrochloric acid trace-metal grade (36 wt %), 98% methanol, and 99% *n*-butanol were purchased from Sigma Aldrich, and 99.999% bismuth(III) oxide, 99.999% antimony(III) oxide, 99% hydrazine monohydrate, and 99% *n*-octane were purchased from Alfa Aesar. The 65-wt % trace-metal-grade nitric acid was obtained from Fisher Scientific. Elemental bismuth and antimony with 99.999% purity were obtained from 5N Plus. All reagents were used as received.

B. Synthesis

1. Bulk polycrystalline $Bi_{1-x}Sb_x$ compounds by ingot casting and quenching

A series of $Bi_{1-x}Sb_x$ bulk polycrystalline samples with $x = 0.03$, 0.04, 0.05, and 0.06 are prepared with a melting-quenching procedure. Bulk 99.999% Bi and 99.999% Sb are weighed to stoichiometry, and approximately 10 g of material is loaded into a quartz ampoule. The ampoule is then sealed under vacuum and heated in a furnace at 800°C for 8 h, with frequent shaking. Subsequently, the melts are cooled to 350°C, followed by quenching in water to minimize phase segregation. For transport measurement, the as-quenched ingots are cut into parallelepipeds with dimensions of about $7 \times 2 \times 1.5\ mm^3$ using a diamond saw.

2. Bulk polycrystalline $Bi_{1-x}Sb_x$ compounds by wet-chemistry route

Bulk $Bi_{1-x}Sb_x$ samples with $x = 0.02$, 0.04, and 0.10 are prepared by dissolving appropriate amounts of Bi_2O_3 and Sb_2O_3 in 36-vol % hydrochloric acid and subsequently hydrolyzing the obtained precursor solution in distilled water. The precipitate is collected through filtration and dried at room temperature. Next, the Bi-Sb precursor is reduced to remove all oxygen and chloride from the precursor at 230 °C for 12 h in a flow of hydrazine vapor

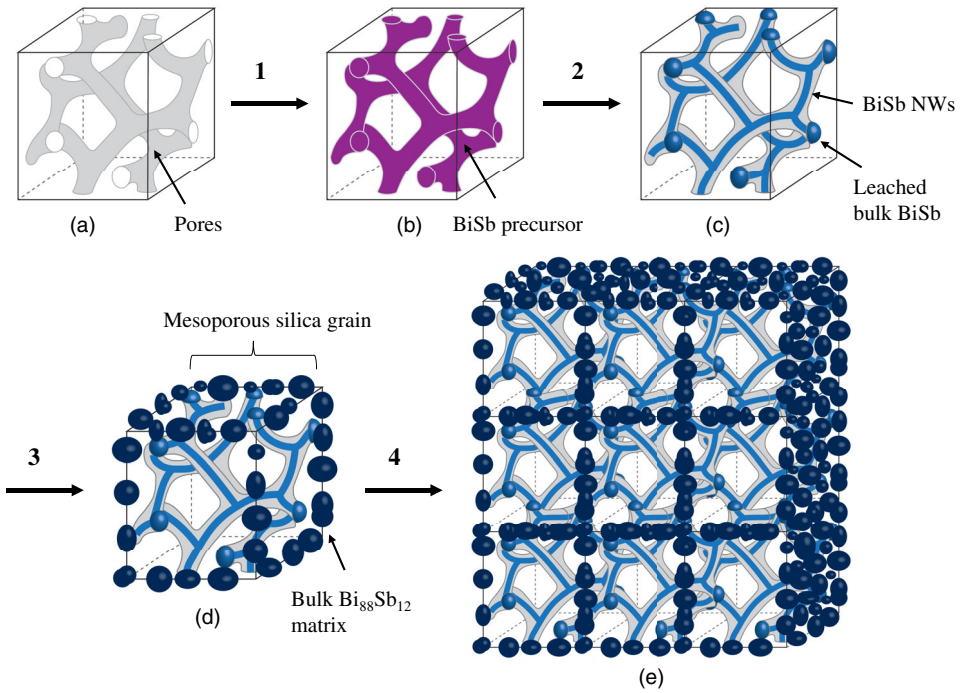

FIG. 1. Schematic representation of the synthesis procedure of bulk $Bi_{1-x}Sb_x$ nanowire composite samples starting from the porous silica in (a). The different steps toward the end product consist of (1) impregnation of the aqueous Bi-Sb precursor solution into the template's pores, (2) reduction of the Bi-Sb precursor to metallic Bi-Sb, (3) mixing of the nanocomposite powder with a resistive $Bi_{88}Sb_{12}$ matrix, and (4) SPS sintering of the nanocomposite powder into a bulk-sized sample. The different intermediate products are (a) mesoporous silica grain with tunable pore diameters from 2 to 50 nm, a typical density of 30%, and an interconnected pore structure that allows better percolation between the nanowires. (b) Mesoporous silica with a mixture of $BiCl_3$ and $SbCl_3$ deposited in the pores. (c) Mesoporous silica with metallic Bi-Sb inside its pores. (d) Bi-Sb nanowire composite mixed with $Bi_{88}Sb_{12}$ matrix. (e) Bulk-sized sample containing nanowires embedded in the silica pores. Note that Bi-Sb leaches partially outside the pores during the reduction treatment, which is shown in (c). To help with sintering while minimizing the effects of electrical short circuits through the leached material, a resistive matrix of $Bi_{88}Sb_{12}$ is added.

carried by N_2-5% H_2 gas. During the low-temperature reduction treatment of the precursor, a mixture of elemental Bi, Sb, and Bi-Sb phase are obtained. $Bi_{1-x}Sb_x$ samples are obtained by sintering the Bi-Sb powders at 245 °C for 90 min at 30 MPa under vacuum using a spark plasma sintering (SPS) device. The compacted disks are cut into parallelepipeds with dimensions of approximately $7 \times 2 \times 1.5$ mm^3 using a diamond saw for transport measurements.

3. $Bi_{1-x}Sb_x$ *nanocomposites by wet-chemistry route*

$Bi_{1-x}Sb_x$ nanowire composite samples with $x = 0.03$ and 0.06 are prepared according to the process depicted in Fig. 1. First, the pores of a mesoporous silica template are impregnated with a mixture of bismuth and antimony salts, followed by the reduction of the salts to remove all Cl and O, yielding a mixture of elemental Bi, Sb, and $Bi_{1-x}Sb_x$. Next, the nanocomposite powder is mixed with bulk $Bi_{88}Sb_{12}$, which promotes sintering while simultaneously acting as a resistive matrix by filling the voids between adjacent silica grains and presenting an energy gap much larger than that of the $x = 0.03$ or 0.06 material. Finally, bulk-sized samples composed of $Bi_{1-x}Sb_x$ nanowires are obtained by sintering the nanocomposite powder using a SPS device.

The mesoporous silica template, pore-expanded FDU-12 (Fudan University–type mesoporous materials), is synthesized according to Ref. [36], while SBA-16 (Santa Barbara amorphous-type material) is prepared as reported in Ref. [37]. The amounts of precursor impregnated into the template's pores are based on the quantities of precursor required to fill the pores completely with $BiCl_3$ and $SbCl_3$. Typically, an excess of precursors is added since the $BiCl_3$ precursor salt decomposes to denser (Bi,O)Cl during the impregnation, allowing a higher pore filling with (Bi,O)Cl compared to $BiCl_3$. As a reference, when the pores are filled completely with $BiCl_3$, the reduced samples can yield up to 32-vol % Bi nanowires within the template's pores, whereas that value can be as high as 60 vol % when the pores are completely filled with (Bi,O)Cl. After filling the pores with $Bi_{94}Sb_6$ or $Bi_{97}Sb_3$ precursor, the nanocomposite powders are mixed with 10- to 25-vol % bulk polycrystalline $Bi_{88}Sb_{12}$. The continuous-feed nanocasting process used to impregnate the template's pores with an aqueous precursor solution is detailed in Ref. [35]. A schematic of the setup is shown in Fig. 2.

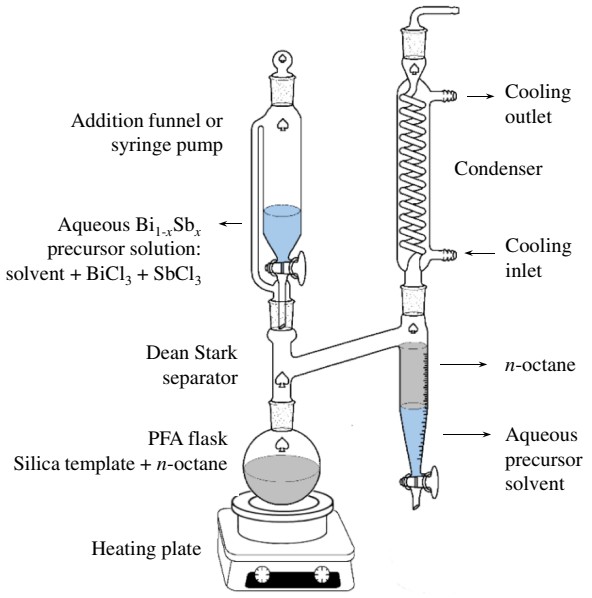

FIG. 2. Continuous-feed nanocasting setup used to impregnate the mesoporous silica's pores. The setup consists of a heating plate, a round-bottom flask, a Dean Stark separator, an addition system, such as a syringe pump, and a condenser. The silica template and *n*-octane are brought into the PFA flask and connected with the Dean Stark separator and the addition system. First, the temperature is increased to 165 °C, allowing the nonpolar solvent to boil. Second, the precursor solution is added at a rate of 4 mL/h and infiltrates the pores through capillary impregnation. Next, the immiscible aqueous phase is separated from the *n*-octane based on difference in density. Consequently, the process allows the deposition of $BiCl_3$ and $SbCl_3$ metal salts inside the template's pores, starting from a diluted precursor solution.

In a typical synthesis of $Bi_{94}Sb_6$ nanocomposites, 1 g of FDU-12 mesoporous silica powder with a Barrett-Joyner-Halenda (BJH) pore volume of 0.9 cm^3/g and a pore diameter of approximately 1525 nm is dispersed in 100 mL of octane and brought into a 250-mL perfluoroalkoxy alkane polymer (PFA) round-bottom flask equipped with a Dean Stark separator and condenser. The recipient is heated to 165 °C to enable the solvent to reflux gently. The $Bi_{94}Sb_6$ precursor solution is prepared by dissolving 5.8646 g of Bi_2O_3 (12.6 mmol) and 0.2342 g of Sb_2O_3 (0.8 mmol) in 21 mL of 36-wt % hydrochloric acid and diluting with 5 mL of water, 13 mL of formic acid, and 120 mL of methanol. The solution is injected into the PFA flask at a rate of 4 mL/h using a syringe pump. The template's pores are considered completely filled upon the addition of an excess of 200% $Bi_{94}Sb_6$ precursor solution based on the supposition that the addition of any further precursor solution will lead only to deposition of precursor salt on the template's exterior surface. The voids between the $Bi_{94}Sb_6$-silica grains are filled deliberately with a resistive matrix of $Bi_{88}Sb_{12}$ by adding an excess of $Bi_{88}Sb_{12}$ precursor solution. As the template's pores already are filled with the $Bi_{94}Sb_6$ precursor, it is assumed that the $Bi_{88}Sb_{12}$ precursor is deposited on the $Bi_{94}Sb_6$-silica grains' exterior surface. The amount of $Bi_{88}Sb_{12}$ accounts for 10 vol % of the total volume.

$Bi_{97}Sb_3$ nanocomposites are synthesized using the SB-16 mesoporous silica template with a pore diameter between 25 and 35 nm and a pore volume of 1.3 cm^3/g. An excess of 160% precursor salt is impregnated into the template, consisting of 6.8101 g of Bi_2O_3, 0.2720 g of Sb_2O_3, 25 mL of 36-wt % HCl, 25 mL of H_2O, and 25 mL of formic acid, while 25-vol % $Bi_{88}Sb_{12}$ matrix is added (4.7848 g of Bi_2O_3 and 0.4082 g of Sb_2O_3).

The as-synthesized nanocomposite powders are collected through filtration, washed with hexane, and subjected to the reduction treatment discussed earlier for bulk wet-chemistry-synthesized $Bi_{1-x}Sb_x$. Bulk nanocomposite samples are formed by SPS sintering the powders as we mention above. Note that all processes, including cutting the sample, sample mounting, and transport measurements, are conducted under air-free conditions to prevent any oxidation of the nanowires [35].

C. Characterization

X-ray powder diffraction (XRD) (Fig. 3) patterns are recorded on a Rigaku MiniFlex diffractometer with the

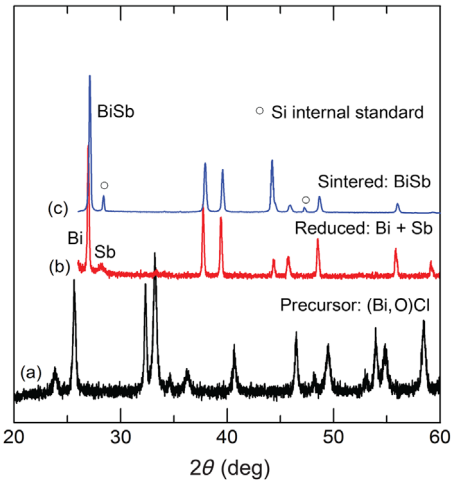

FIG. 3. Normalized XRD patterns of (a) the Bi-Sb precursor embedded in the silica template, (b) the reduced samples, and (c) SPS sintered samples. (a) Upon impregnating the mesoporous silica template with a mixture of $BiCl_3$ and $SbCl_3$, the precursor salts hydrolyze with the formation of (Bi,O)Cl. Neither $SbCl_3$ nor (Sb,O)Cl are detected, which may be due to low content or their presence as an amorphous phase or phases. (b) The reduced samples are obtained by treating the powders at 230 °C in a flow of N_2, 5% H_2 saturated with hydrazine hydrate vapor for 12 h. The diffraction peaks of elemental Bi and Sb can be observed as indicated in the figure. (c) $Bi_{1-x}Sb_x$ alloys are formed during the SPS sintering process at 245 °C for 90 min, as can be seen from the shift in 2θ values and absence of elemental Sb, and 10-wt % Si is added as internal standard to confirm the peak shift is due to alloying.

Bragg-Brentano θ-2 θ configuration and using Cu $K\alpha$ radiation. Nitrogen-sorption experiments are performed at 77 K with a Micromeritics TriStar 3000 device. Samples are vacuum dried at 180 °C for 12 h prior to analysis. The pore-size distribution, and, consequently, the pore diameter, are determined by analysis of the adsorption branch of the isotherms using the BJH method (procedure for calculating pore size distributions from experimental isotherms using the Kelvin model of pore filling). X-ray-fluorescence measurements are performed on a Rigaku NEX CG device. The sample compositions are analyzed by dissolving small pieces of samples into 3:1 hydrochloric acid–nitric acid. The recorded intensities are related to their composition using a calibration curve.

Galvanomagnetic and thermomagnetic properties (including thermopower, resistivity, Hall coefficient, and Nernst coefficient) are measured in a self-built cryostat from 80 to 400 K using the method described in Ref. [38]. Thermal conductivity is measured using a steady-state heat-sink method. Mobility is calculated from the measured resistivity and Hall coefficient. The error in the thermopower mainly results from electrical noise in voltage and thermocouples because the mounting ensures that the temperature and voltage differences are measured at the same point. Two copper-constantan thermocouples are attached to the sample with silver epoxy; the attachment spot is made intentionally small to minimize error in the thermopower measurement estimated to be approximately 3%. The errors in the resistivity, Hall coefficient, and Nernst coefficient mainly come from geometric uncertainties. The error in the Hall coefficient and Nernst coefficient is estimated to be 5% and the error in resistivity 10%. The error in thermal conductivity comes from two sources: geometric uncertainty and radiation heat loss, which is measured in a cryostat without the sample as a function of temperature. The samples have a relatively high thermal conductivity, and the measurements are cut off at the temperature at which it is estimated that the radiation loss is approximately 10% of the sample conductance. To this radiation loss, one adds the geometric uncertainty of also approximately 10%. Note that the geometric uncertainty in thermal conductivity and in electrical resistivity will compensate each other when calculating zT.

III. GALVANOMAGNETIC AND THERMOMAGNETIC DATA

In this section, the galvanomagnetic and thermomagnetic properties of cast ingots and wet-chemistry-prepared $Bi_{1-x}Sb_x$ alloys are compared. Figure 4(a) shows the temperature dependence of the resistivity of bulk polycrystalline cast ingots of $Bi_{1-x}Sb_x$ with $x = 3, 4, 5$, and 6 at. %, which are quite similar to the average of the results obtained in the literature [23,24] along the binary and trigonal axes. The chemically prepared polycrystals in Fig. 4(b) for $x = 2$, 4, and 10 at. % are more resistive by a factor of approximately 2 at room temperature and more at 100 K. The results of the nanowire composites of diameter around 15–25 and 25–35 nm for $x = 3$ and 6 at. % are more resistive by another factor of approximately 5. However, we note that the resistivity is measured using the physical dimensions of the composite, and it is not corrected for the volume fraction of the Bi-Sb material in it. Given that Bi-Sb fills in only about 35 vol % of the template's pore volume, while the rest (SiO_2 and voids) does not conduct, roughly a factor of 2 from the total increase in resistivity is simply due to the geometric effect.

To analyze further the origin of these temperature dependences, low-field (i.e., at field where the product of mobility and magnetic induction is below unity, $\mu B < 1$) Hall effect data are taken. For the nanocomposites, the Hall resistivity is corrected for the volume fractions of Bi-Sb by using the effective-medium theory [39] for the Hall effect; for a 35% Bi-Sb filling by volume, that correction is a factor of 2. It is known that the Hall and magnetoresistance data of elemental Bi are the result of the contributions of both electrons and holes, necessitating a complicated fit to obtain electron and hole concentrations and mobilities separately [40]. However, the semiconducting Bi-Sb alloys can, in principle, be treated as a single n-type carrier system, and the carrier concentration then becomes the inverse of the Hall constant R_H times the electron charge e.

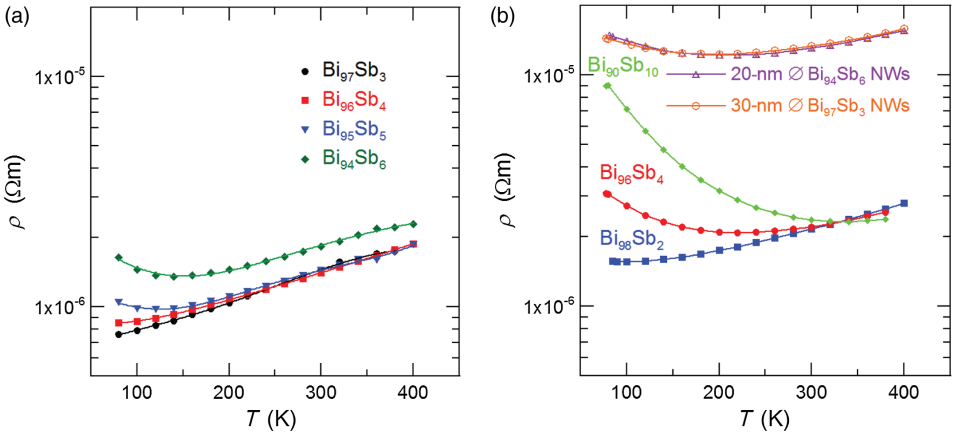

FIG. 4. Temperature dependence of the resistivity of (a) polycrystalline cast ingots of $B_{1-x}Sb_x$ alloys of the compositions indicated. Frame (b) shows the same quantity measured on polycrystals sintered from powders prepared using the same wet chemistry as for the nanowire composites. The chemically synthesized $Bi_{1-x}Sb_x$ nanocomposites are labeled by their wire diameter and composition, while the equivalent bulk samples are labeled by their compositions only.

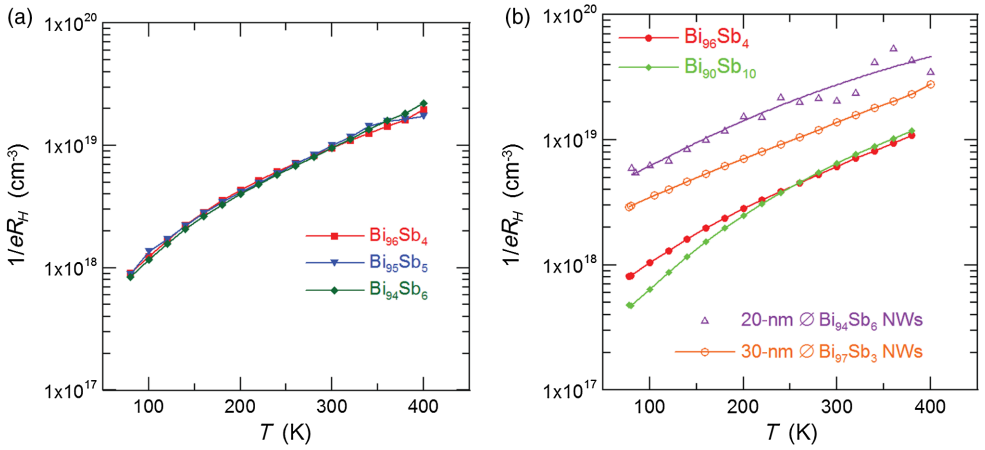

FIG. 5. Temperature dependence of the inverse of the low-field Hall coefficient of (a) polycrystalline cast ingots of semiconducting $B_{1-x}Sb_x$ alloys ($x > 0.04$) of the compositions indicated. Frame (b) shows the same quantity measured on polycrystals sintered from powders prepared using the same wet chemistry as for the nanowire composites. The chemically synthesized $Bi_{1-x}Sb_x$ nanocomposites are labeled by their wire diameter and composition, while the equivalent bulk samples are labeled by their compositions only.

This quantity is represented in Fig. 5 for samples of a composition such that they are semiconducting. The carrier concentration increases monotonically with the temperature, the classical behavior of narrow-gap semiconductors, and the model should hold at least up to 150–200 K given the projected values for the band gaps. From this carrier concentration and the resistivity in Fig. 4, one can derive the electron mobilities in the different samples, which are reported in Fig. 6. The mobility of the bulk ingots at liquid N_2 temperature is roughly 50% higher than that of the bulk samples prepared by wet chemistry and become comparable around room temperature; that of the nanowire composites are approximately 1 order of magnitude lower than bulk samples prepared by wet chemistry. For the resistivity, a factor of 2 of that ratio is due to geometry alone (a calculation of the purely geometric effects based on the effective-medium theory is presented in the Supplemental Material [1]).

In the high-temperature regime where $d\rho/dT > 0$, the temperature dependence of the resistivity is due to the decrease in mobility with increasing temperature, an indication of the presence of electron-acoustic phonon scattering over the increase in electron concentration. In the temperature range where $d\rho/dT < 0$, the temperature dependence of the resistivity is dominated by the increase in carrier concentration, presumably by thermal excitations of the carriers across the energy gap.

The total thermal conductivity is shown in Fig. 7. For the bulk ingots, the order of magnitude of the electronic contribution can be estimated from the Wiedemann-Franz-Lorenz law using the free-electron Lorenz number to be of the order of 2 W/mK at 100 K and >4 W/mK at 300 K. For the bulk samples prepared with wet-chemical methods, values > 3 W/mK are estimated at 300 K, but much less for the 4% and 10% Sb samples at 100 K. It is known that ambipolar conduction dominates the thermal conduction in semimetallic Bi at 200 K [10]. The samples studied here are narrow-gap semiconductors so that the ambipolar conduction should be much lower, but it cannot be dismissed at the temperatures where the samples essentially become intrinsic semiconductors. Separating the ambipolar term requires knowledge of the partial conductivities and thermopowers of both electrons and holes for which we have too few data in polycrystals (Ref. [10] used single crystals of two separate orientations, together with assumptions about the band structure.) It is

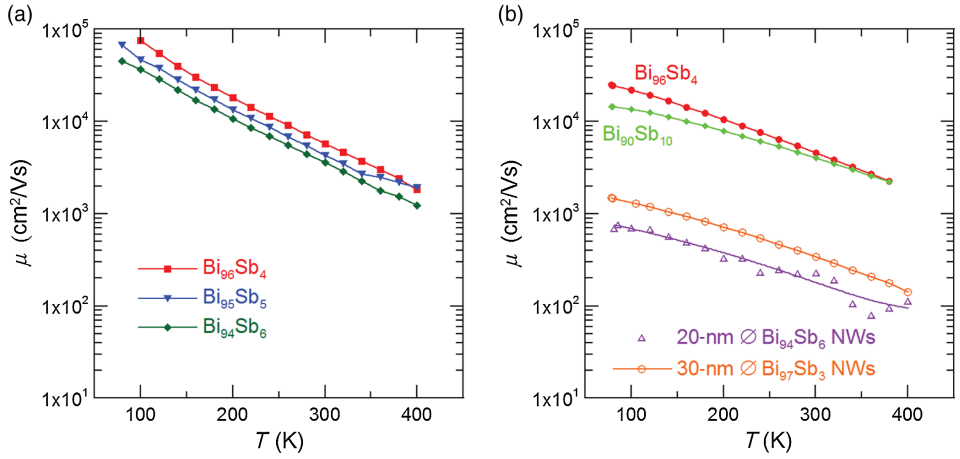

FIG. 6. Temperature dependence of the electron mobility of (a) polycrystalline cast ingots of semiconducting $B_{1-x}Sb_x$ alloys ($x > 0.04$) of the compositions indicated. Frame (b) shows the same quantity measured on polycrystals sintered from powders prepared using the same wet chemistry as for the nanowire composites. The chemically synthesized $Bi_{1-x}Sb_x$ nanocomposites are labeled by their wire diameter and composition, while the equivalent bulk samples are labeled by their compositions only.

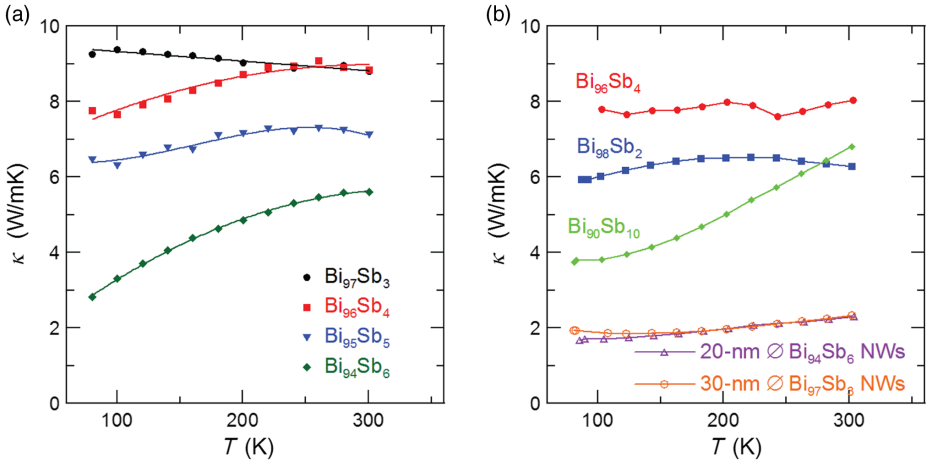

FIG. 7. Temperature dependence of the thermal conductivity of (a) polycrystalline cast ingots of $B_{1-x}Sb_x$ alloys of the compositions indicated. Frame (b) shows the same quantity measured on polycrystals sintered from powders prepared using the same wet chemistry as for the nanowire composites. The chemically synthesized $Bi_{1-x}Sb_x$ nanocomposites are labeled by their wire diameter and composition, while the equivalent bulk samples are labeled by their compositions only.

clear from the numbers above that the thermal conductivity of the bulk ingots at all temperatures and that of the 4% and 10% Sb ingots prepared by wet chemistry at 300 K has a very substantial electronic contribution. The thermal conductivity of the nanowire composites remains nearly temperature independent at 2 W/mK. Since that of the SiO_2 is of the order of 0.2 W/mK and the Bi-Sb fills about 35 vol % of the sample, it appears that the thermal conductivity of the Bi-Sb in the pores dominates the measured values. The thermal short through the porous host material, which had affected the zT of nanowire array samples in the past [19], is apparently less of a problem in this material. This is probably because the fraction of the pores filled by Bi-Sb nanowires that are electrically in contact with each other is much improved by the present wet-chemical method and by the multiple connectivity of the host material's channels.

Most interesting are the thermopower results given in Fig. 8. It is known that the TE power of elemental Bi [10] and of the semimetallic $Bi_{1-x}Sb_x$ alloys [23] is anisotropic,

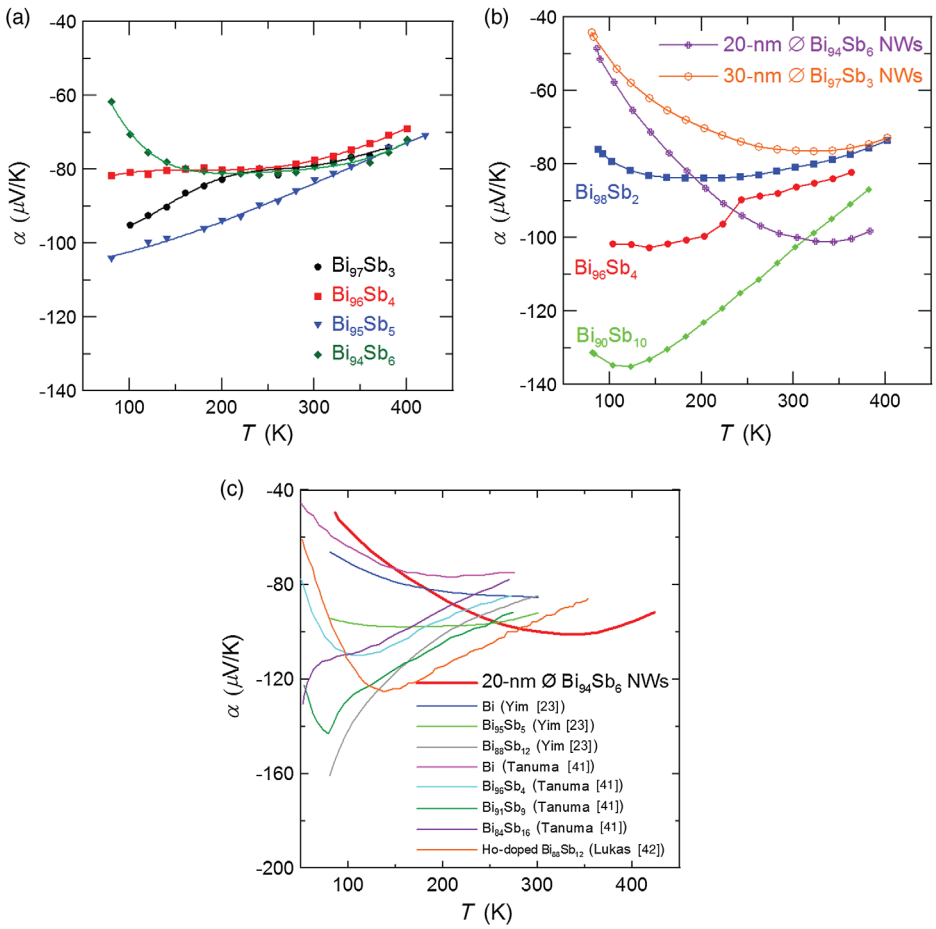

FIG. 8. Temperature dependence of the Seebeck coefficient of (a) polycrystalline cast ingots of $B_{1-x}Sb_x$ alloys of the compositions indicated. Frame (b) shows the same quantity measured on polycrystals sintered from powders prepared using the same wet chemistry as for the nanowire composites. The chemically synthesized $Bi_{1-x}Sb_x$ nanocomposites are labeled by their wire diameter and composition, while the equivalent bulk samples are labeled by their compositions only. Frame (c) compares the Seebeck coefficient of the 20-nm-diameter NW composites of $Bi_{94}Sb_6$ with values collected from the literature for the various Bi-Sb alloys labeled. The references are Yim [23], Tanuma [41], and Lukas [42].

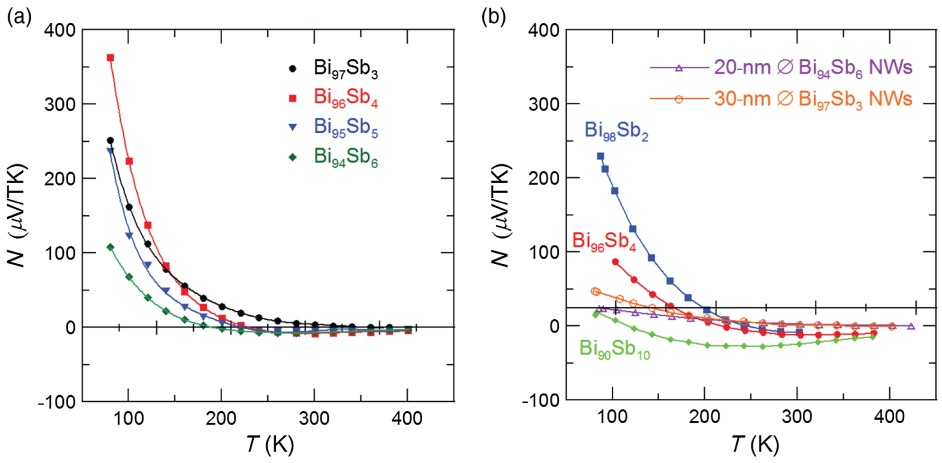

FIG. 9. Temperature dependence of the low-field Nernst coefficient of (a) polycrystalline cast ingots of $B_{1-x}Sb_x$ alloys of the compositions indicated. Frame (b) shows the same quantity measured on polycrystals sintered from powders prepared using the same wet chemistry as for the nanowire composites. The chemically synthesized $Bi_{1-x}Sb_x$ nanocomposites are labeled by their wire diameter and composition, while the equivalent bulk samples are labeled by their compositions only.

with the thermopower along the c-axis $\alpha_{//}$ as much as twice the in-plane thermopower $\alpha_{\perp}$. In contrast, the thermopower of the semiconducting alloys ($x = 12$, 15, and 18 at. %) [23] is more isotropic. Since this manuscript concerns polycrystals, it is assumed that the thermopower α shown in Fig. 8 is an average given by $\alpha = \frac{2}{3}\alpha_{\perp} + \frac{1}{3}\alpha_{//}$. The thermopower reported for the cast ingots and the bulk samples prepared by wet chemistry all follow the values reported in the literature [23] for their respective values of x. The low-temperature value reported for $x = 0.1$ [Fig. 8(b)] is the highest reported here, but is also quite usual at that concentration [23]. Generally, as the temperature increases to and above room temperature, the thermopower of all samples converge to a value between −50 and −80 μV/K, probably because k_BT approaches the energies of the details of $E_{gLsa}(T)$, $E_{gTLs}(T)$, and $E_{gTLa}(T)$.

In contrast, the thermopower of the 20-nm-diameter nanocomposite sample of $Bi_{96}Sb_6$ maintains a thermopower with an absolute value in excess of 100 μV/K from 300 to 380 K [see Fig. 8(b)]. A comparison of the thermopower of this polycrystalline sample with literature values given in Fig. 8(c) shows that, to our knowledge, this value has not been equaled previously by Sb alloying of Bi alone. This change in thermopower also cannot result from an effective-medium effect, which is calculated in the Supplemental Material [1]. The sample has a quite high carrier concentration (2 to 3×10^{19} cm^{-3}) and mobility (200 to 100 cm^2/Vs) in that temperature range, indicating band conduction. The thermopower is also much larger than what can be achieved with $Bi_{88}Sb_{12}$, indicating that the effect cannot be due to the material in the channels between the nanowires. Therefore, we suggest that size quantization increases the gap of this material above what is possible with Sb alloying.

The Nernst effect is typically larger than the Seebeck effect at moderate magnetic fields (i.e., $\mu B \sim 1$) in semimetals [43] in general and in Bi in particular [44] because the contributions of electrons and holes are additive. The low-field adiabatic Nernst coefficients N (i.e., the slope of the transverse thermopower with field) of the alloys measured here are given in Fig. 9 and generally confirm the conclusions. N decreases as x is increased, but it is generally quite large with $N \times 1\ \mathrm{T} > |\alpha|$ at 100 K (specifically, $N \times 1\ \mathrm{T} \sim 350$ to 100 μV/K, whereas $\alpha \sim -50$ to −120 μV/K) in semimetallic samples for $x < 0.08$, while the reverse is true at $x = 0.1$. The exceptions are the nanowire composites, which behave like the semiconducting samples.

The thermoelectric power factor $\mathrm{PF} \equiv \alpha^2/\rho$ and figure of merit $zT \equiv \alpha^2 T/\rho\kappa$ are calculated from the above data and reported in Figs. 10 and 11, respectively. It is known [23,24] that power factors of the bulk single-crystal $Bi_{1-x}Sb_x$ alloys along the trigonal direction reach 100 μW/cm K^2, far exceeding those of the tetradymites [2]. The present results extend that to polycrystals. The relatively lower zT of $Bi_{1-x}Sb_x$ alloys compared to tetradymites is due to their high lattice thermal conductivity and modest Seebeck coefficient. The fact that the present samples are polycrystals is a second major disadvantage inherent in nanocomposites, since, as outlined in the Introduction, the best zT ($\leq$0.7) values are achieved in trigonal crystals doped with the resonant impurity potassium. However, from a practical standpoint, polycrystalline samples are preferred over single crystals since they are mechanically stronger and easier to synthesize. In addition, the values obtained for the nanowire composites in Fig. 10 are orders of magnitude better than those measured on previous Bi nanocomposites [19]. According to calculations by Rabin *et al.* [45], n-type $Bi_{85}Sb_{15}$ nanowires with a diameter of 20 nm have the potential to reach zT values as high as 2.5, which will drastically enhance the efficiency of thermoelectric solid-state cooling devices and make them competitive with vapor-compression-based cooling systems. However, Cornett and Rabin [46] reported that the extent of the zT enhancement in nanowire thermoelectrics also depends on single-band versus multisubband transport, which previously was not considered and makes the expected zT arguable.

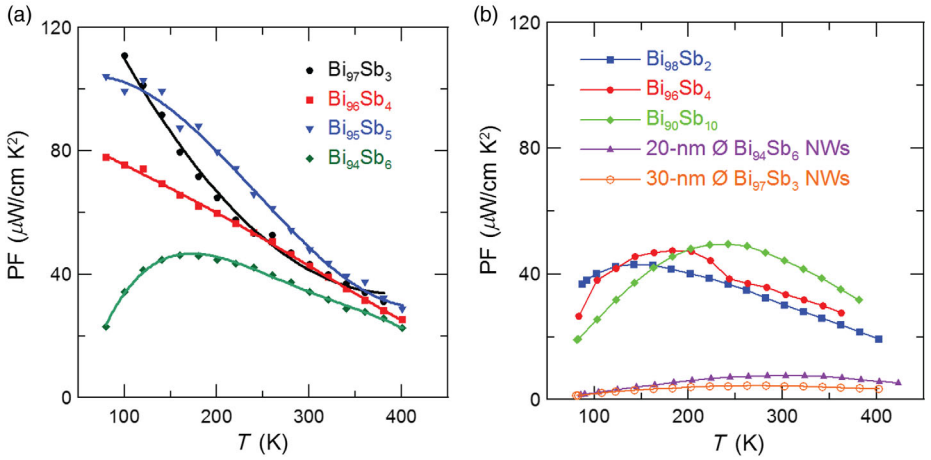

FIG. 10. Temperature dependence of the thermoelectric power factor of (a) polycrystalline cast ingots of $Bi_{1-x}Sb_x$ alloys of the compositions indicated. Frame (b) shows the same quantity measured on polycrystals sintered from powders prepared using the same wet chemistry as for the nanowire composites. The chemically synthesized $Bi_{1-x}Sb_x$ nanocomposites are labeled by their wire diameter and composition, while the equivalent bulk samples are labeled by their compositions only.

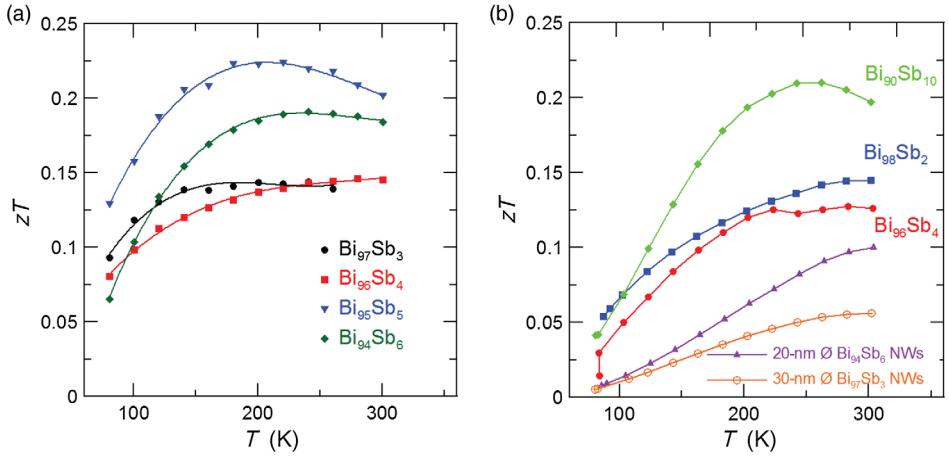

FIG. 11. Temperature dependence of the thermoelectric figure of merit zT of (a) polycrystalline cast ingots of $Bi_{1-x}Sb_x$ alloys of the compositions indicated. Frame (b) shows the same quantity measured on polycrystals sintered from powders prepared using the same wet chemistry as for the nanowire composites. The chemically synthesized $Bi_{1-x}Sb_x$ nanocomposites are labeled by their wire diameter and composition, while the equivalent bulk samples are labeled by their compositions only.

IV. CONCLUSIONS

The wet-chemical method presented here enables the preparation of nanowire composites of semiconducting $Bi_{1-x}Sb_x$ alloys that previous nanowire impregnation methods (vapor deposition and high-pressure liquid injection) could not. Both a reduction of the nanowire diameter and the increase of Sb concentration x (up to 18%) are ways to potentially transform the semimetal Bi into a thermoelectrically relevant Te-free semiconductor. In the present work, both effects are used together. The work shows experimentally that 300-K thermopower values can be obtained in 20-nm $Bi_{94}Sb_6$ nanowire composites that exceed the thermopower of bulk polycrystals of any Sb concentration. Although smaller than the zT of single crystals of Bi-Sb, and particularly ones resonantly doped with K, the zT values reported here are much improved over those obtained on nanocomposites in the past. This is because the wet-chemical method fills the pores better than the vapor-deposition or high-pressure liquid-injection methods. The improvement comes from the fact that a much larger fraction of the Bi-Sb nanowires is in electrical contact with one another in these composites than in those prepared in the past [19]. Further research involves the optimization of the alloy composition and the carrier concentration of the nanowires to maximize their zT.

ACKNOWLEDGMENTS

This work is supported by the U.S. National Science Foundation Grant No. EFRI-2DARE 1433467, as well as by IWT and FWO grants, Flanders, Belgium.

[1] See Supplemental Material at http://link.aps.org/supplemental/10.1103/PhysRevApplied.9.024020. The Supplemental Material has two sections. In the first, we derive the condition under which active cooling (e.g., with a Peltier cooler) results in a more compact heat-exchange system than passive cooling; i.e., we derive Eq. (1). The second part gives effective-medium calculations of the thermoelectric power and resistivity and thermal conductivity of the Bi-Sb and alumina composites.

[2] J. P. Heremans, R. J. Cava, and N. Samarth, Tetradymites as thermoelectrics and topological insulators, Nat. Rev. Mater. **2**, 17049 (2017).

[3] *AMS Alloy Phase Diagram Database*, edited by H. Okamoto and K. Cenzual (ASM International, Metals Park, OH, 2016).

[4] L. D. Hicks and M. S. Dresselhaus, Effect of quantum-well structures on the thermoelectric figure of merit, Phys. Rev. B **47**, 12727 (1993).

[5] L. D. Hicks and M. S. Dresselhaus, Thermoelectric figure of merit of a one-dimensional conductor, Phys. Rev. B **47**, 16631 (1993).

[6] M. Maltz and M. S. Dresselhaus, Magnetoreflection studies in bismuth, Phys. Rev. B **2**, 2877 (1970); M. P. Vecchi and M. S. Dresselhaus, Magnetic energy levels of bismuth in the low-quantum-number limit, Phys. Rev. B **9**, 3257 (1974).

[7] M. P. Vecchi, J. R. Pereira, and M. S. Dresselhaus, Anomalies in the magnetoreflection spectrum of bismuth in the low-quantum-number limit, Phys. Rev. B **14**, 298 (1976).

[8] M. P. Vecchi and M. S. Dresselhaus, Temperature dependence of the band parameters of bismuth, Phys. Rev. B **10**, 771 (1974).

[9] V. S. Edel'man, Properties of electrons in bismuth, Usp. Fiz. Nauk **123**, 257 (1977) [Sov. Phys. Usp. **20**, 819 (1977)].

[10] C. F. Gallo, B. S. Chandrasekhar, and P. H. Sutter, Transport properties of bismuth single crystals, J. Appl. Phys. **34**, 144 (1963).

[11] Y. M. Lin, X. Sun, and M. S. Dresselhaus, Theoretical investigation of thermoelectric transport properties of cylindrical Bi nanowires, Phys. Rev. B **62**, 4610 (2000).

[12] J. P. Heremans, M. S. Dresselhaus, L. Bell, and D. T. Morelli, When thermoelectrics reached the nanoscale, Nat. Nanotechnol. **8**, 471 (2013).

[13] Z. Zhang, D. Gekhtman, M. S. Dresselhaus, and J. Y. Ying, Processing and characterization of single-crystalline ultrafine bismuth nanowires, Chem. Mater. **11**, 1659 (1999).

[14] J. P. Heremans, C. M. Thrush, and D. T. Morelli, Enhanced thermoelectric power in bismuth nanocomposites, U.S. Patent No. 6,670,539 (30 December 2003).

[15] J. P. Heremans, C. M. Thrush, Y. M. Lin, S. Cronin, Z. Zhang, M. S. Dresselhaus, and J. F. Mansfield, Bismuth nanowire arrays: Synthesis and galvanomagnetic properties, Phys. Rev. B **61**, 2921 (2000).

[16] Y. M. Lin, S. B. Cronin, J. Y. Ying, M. S. Dresselhaus, and J. P. Heremans, Transport properties of Bi nanowire arrays, Appl. Phys. Lett. **76**, 3944 (2000).

[17] J. P. Heremans and C. M. Thrush, Thermoelectric power of bismuth nanowires, Phys. Rev. B **59**, 12579 (1999).

[18] J. P. Heremans, C. M. Thrush, and D. T. Morelli, Thermoelectric Power of Bismuth Nanocomposites, Phys. Rev. Lett. **88**, 216801 (2002).

[19] J. P. Heremans, Low-dimensional thermoelectricity, Acta Phys. Pol. A **108**, 609 (2005).

[20] M. Murata, D. Nakamura, Y. Hasegawa, T. Komine, T. Taguchi, S. Nakamura, C. M. Jaworski, V. Jovovic, and J. P. Heremans, Mean free path limitation of thermoelectric properties of bismuth nanowire, J. Appl. Phys. **105**, 113706 (2009).

[21] S. Tang and M. S. Dresselhaus, Phase diagrams of $Bi_{1-x}Sb_x$ thin films with different growth orientations, Phys. Rev. B **86**, 075436 (2012).

[22] L. Fu and C. L. Kane, Topological insulators with inversion symmetry, Phys. Rev. B **76**, 045302 (2007).

[23] W. M. Yim and A. Amith, BiSb alloys for magneto-thermoelectric and thermomagnetic cooling, Solid State Electron. **15**, 1141 (1972).

[24] B. Lenoir, M. Cassart, J.-P. Michenaud, H. Scherrer, and S. Scherrer, Transport properties of Bi-rich Bi-Sb alloys, J. Phys. Chem. Solids **57**, 89 (1996); B. Lenoir, A. Dauscher, X. Devaux, R. Martin-Lopez, I. Y. Ravich, H. Scherrer, and S. Scherrer, in *Proceedings of the 15th International Conference on Thermoelectrics*, 1996, pp. 1–13 (unpublished).

[25] J. P. Heremans, H. Jin, Y. H. Zheng, S. J. Watzman, and A. Prakash, BiSb and spin-related thermoelectric phenomena, Proc. SPIE Int. Soc. Opt. Eng. **9821**, 982117 (2016); J. P. Heremans and H. Jin, Thermoelectric and spin-caloritronic coolers: from basics to recent developments, Proc. SPIE Int. Soc. Opt. Eng. **9765**, 976507 (2016).

[26] H. Jin, B. Wiendlocha, and J. P. Heremans, *P*-type doping of elemental bismuth with indium, gallium and tin: A novel doping mechanism in solids, Energy Environ. Sci. **8**, 2027 (2015).

[27] H. Jin, C. M. Jaworski, and J. P. Heremans, Enhancement in the figure of merit of *p*-type $Bi_{1-x}Sb_x$ alloys through multiple valence-band doping, Appl. Phys. Lett. **101**, 053904 (2012).

[28] K. Scholtz, P. Jandl, U. Birkholz, and Z. M. Dashevskii, Infinite stage Ettingshausen cooling in Bi-Sb alloys, J. Appl. Phys. **75**, 5406 (1994).

[29] P. Jandl and U. Birkholz, Thermogalvanomagnetic properties of Sn-doped $Bi_{95}Sb_5$ and its application for solid state cooling, J. Appl. Phys. **76**, 7351 (1994).

[30] S. Tang and M. S. Dresselhaus, Phase diagrams of $Bi_{1-x}Sb_x$ thin films with different growth orientations, Phys. Rev. B **86**, 075436 (2012).

[31] S. Tang and M. S. Dresselhaus, Electronic phases, band gaps, and band overlaps of bismuth antimony nanowires, Phys. Rev. B **89**, 045424 (2014); S. Tang and M. S. Dresselhaus, Electronic properties of nano-structured bismuth antimony materials, J. Mater. Chem. C **2**, 4710 (2014).

[32] Y.-M. Lin, O. Rabin, S. B. Cronin, J. Y. Ying, and M. S. Dresselhaus, Semimetal-semiconductor transition in $Bi_{1-x}Sb_x$ alloy nanowires and their thermoelectric properties, Appl. Phys. Lett. **81**, 2403 (2002).

[33] J. P. Heremans, C. M. Thrush, Y.-M. Lin, S. B. Cronin, and M. S. Dresselhaus, Transport properties of antimony nanowires, Phys. Rev. B **63**, 085406 (2001).

[34] J. P. Heremans, C. M. Thrush, D. T. Morelli, and M.-C. Wu, Resistance, Magnetoresistance, and Thermopower of Zinc Nanowire Composites, Phys. Rev. Lett. **91**, 076804 (2003).

[35] K. Vandaele, J. P. Heremans, I. Van Driessche, P. Van Der Voort, and K. De Buysser, Continuous-feed nanocasting process for the synthesis of bismuth nanowire composites, Chem. Commun. (Cambridge) **53**, 12294 (2017).

[36] L. Huang, X. Yan, and M. Kruk, Synthesis of ultralarge-pore FDU-12 silica with face-centered cubic structure, Langmuir **26**, 14871 (2010).

[37] Z. Dongyuan, H. Qisheng, F. Jianglin, F. C. Bradley, and D. S. Galen, Nonionic triblock and star diblock copolymer and oligomeric surfactant syntheses of highly ordered, hydrothermally stable, mesoporous silica structures, J. Am. Chem. Soc. **120**, 6024 (1998).

[38] J. P. Heremans, C. M. Thrush, and D. T. Morelli, Thermopower enhancement in lead telluride nanostructures, Phys. Rev. B **70**, 115334 (2004).

[39] D. J. Bergman and D. G. Stroud, High-field magnetotransport in composite conductors: Effective-medium approximation, Phys. Rev. B **62**, 6603 (2000).

[40] J. P. Heremans and O. P. Hansen, Influence of nonparabolicity on intravalley electron-phonon scattering; the case of bismuth, J. Phys. C **12**, 3483 (1979).

[41] S. Tanuma, Thermoelectric power of bismuth-antimony alloys, J. Phys. Soc. Jpn. **16**, 2354 (1961).

[42] K. C. Lukas, Thermoelectric properties of Ho-doped $Bi_{0.88}Sb_{0.12}$, J. Mater. Sci. **47**, 5729 (2012).

[43] S. J. Watzman, T. M. McCormick, C. Shekhar, S.-C. Wu, Y. Sun, A. Prakash, C. Felser, N. Trivedi, and J. P. Heremans, Dirac dispersion generates large Nernst effect in Weyl semimetals, arXiv:1703.04700.

[44] J. H. Mangez, J.-P. Issi, and J. P. Heremans, Transport properties of bismuth in quantizing magnetic fields, Phys. Rev. B **14**, 4381 (1976).

[45] O. Rabin, Y. Lin, and M. S. Dresselhaus, Anomalously high thermoelectric figure of merit in $Bi_{1-x}Sb_x$ nanowires by carrier pocket alignment, Appl. Phys. Lett. **79**, 81 (2001).

[46] J. E. Cornett and O. Rabin, Thermoelectric figure of merit calculations for semiconducting nanowires, Appl. Phys. Lett. **98**, 182104 (2011).